An Interferometric Reflectance Imaging Sensor for Point of Care Viral Diagnostics

Alexander P. Reddington, *Student Member, IEEE*, Jacob T. Trueb, David S. Freedman, *Member, IEEE*, Ahmet Tuysuzoglu, *Student Member, IEEE*, George G. Daaboul, Carlos A. Lopez, W. Clem Karl, *Senior Member, IEEE*, John H. Connor, Helen Fawcett, and M. Selim Ünlü*, *Fellow, IEEE*

Abstract—The use of *in vitro* diagnostic devices is transitioning from the laboratory to the primary care setting to address early disease detection needs. Time critical viral diagnoses are often made without support due to the experimental time required in today's standard tests. Available rapid point of care (POC) viral tests are less reliable, requiring a follow-on confirmatory test before conclusions can be drawn. The development of a reliable POC viral test for the primary care setting would decrease the time for diagnosis leading to a lower chance of transmission and improve recovery. The single particle interferometric reflectance imaging sensor (SP-IRIS) has been shown to be a sensitive and specific-detection platform in serum and whole blood. This paper presents a step towards a POC viral assay through a SP-IRIS prototype with automated data acquisition and analysis and a simple, easy-to-use software interface. Decreasing operation complexity highlights the potential of SP-IRIS as a sensitive and specific POC diagnostic tool. With the integration of a microfluidic cartridge, this automated instrument will allow an untrained user to run a sample-to-answer viral assay in the POC setting.

Index Terms—Automation, biosensors, label-free, nanoparticle detection, point-of-care, virus detection.

I. INTRODUCTION

POINT of care (POC) diagnostics devices are one of the fastest growing sectors of the medical industry [1]. The rapid market growth in this sector as compared to traditional diagnostic tests is attributed to the paradigm shift toward targeted early disease detection, therapy, and sample-to-answer automation [2]. There are three standard diagnostic tests for viral infections that are performed in core laboratories. Viral cultures have unparalleled sensitivity, but take several days to generate results. Reverse transcriptase polymerase chain reaction assays offer quantitative results with good sensitivity, in few hours, but usually require intensive sample purification and processing [3]. Enzyme-linked immunosorbent assays represent a fairly rapid test with good sensitivity, but the sensitivity is less than the other two methods. For time critical situations, commercially available rapid diagnostic tests for viral infection take the form of lateral flow immunoassays, which suffer from low sensitivity and require production of antibodies against the pathogen [4]. The lack of a sensitive and specific rapid test in the primary care setting requires clinical procedures to include a second confirmatory test in a core laboratory causing delays in diagnosis, prolonged recovery, and an increased chance of transmitting the infection to others [5]. Therefore, the development of a diagnostic platform capable of combining clinically relevant levels of sensitivity and specificity in a physician's office would represent an invaluable tool in the fight against viral diseases.

On the one end of the spectrum, recent innovations in optical biosensors have pushed detection sensitivity to new limits. For example, photonic crystal structures on the sensor surface have been used to amplify the fluorescence signal [6]. Whispering gallery mode biosensors have created a high Q-factor structure to achieve femtomolar and single-molecule sensitivities [7], [8]. These laboratory-based techniques, while sensitive, are hindered by a complex fabrication process, a small sensor surface (interaction volume), and a high noise floor from nonspecific interactions in serum.

On the other end of the spectrum, portable devices utilizing standard microscopy imaging techniques and DNA amplification have been developed for POC applications. Hand-held microscopes have been developed to exploit the growing popularity of smartphones for a compact and inexpensive system [9]–[11]. Microfluidics have been extensively developed to miniaturize the popular and reliable polymerase chain reaction amplification technique [12], [13]. These approaches demonstrate a high level of portability. However, sample purification has yet to mature to allow these techniques to achieve high levels of sensitivity [14].

The interferometric reflectance imaging sensor (IRIS) has been shown to be a high-throughput microarray tool for dynamic monitoring of binding interactions [15], [16]. Recently, a change in the optical path has led the IRIS technique to be

A. P. Reddington, A. Tuyuszoglu, and C. A. Lopez are with the Department of Electrical and Computer Engineering, Boston University, Boston, MA 02215 USA (e-mail: aredding@bu.edu; atuysuz@bu.edu; c1lopez@bu.edu).

J. T. Trueb and H. Fawcett are with the Department of Mechanical Engineering, Boston University, Boston, MA 02215 USA (e-mail: jtrueb@bu.edu; hfawcett@bu.edu).

D. S. Freedman and W. C. Karl are with the Department of Electrical and Computer Engineering and Department of Biomedical Engineering, Boston University, Boston, MA 02215 USA (e-mail: dsf@bu.edu; wckarl@bu.edu).

G. G. Daaboul is with the Department of Biomedical Engineering, Boston University, Boston, MA 02215 USA (e-mail: gdaa1987@bu.edu).

J. H. Connor is with the Department of Microbiology, Boston University, Boston, MA 02215 USA (e-mail: jhconnor@bu.edu).

*M. S. Ünlü is with the Department of Electrical and Computer Engineering and Department of Biomedical Engineering, Boston University, Boston, MA 02215 USA (e-mail: selim@bu.edu).

Color versions of one or more of the figures in this paper are available online at http://ieeexplore.ieee.org.

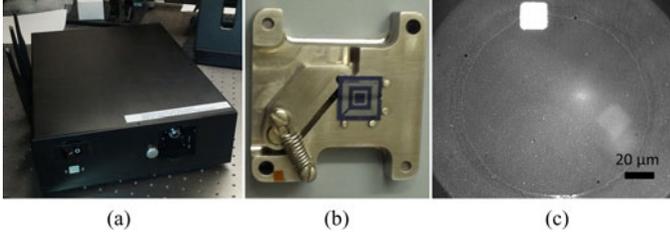Digital Object Identifier 10.1109/TBME.2013.2272666

Fig. 1. (a) Image of the prototype. (b) Patterned chip loaded into the sample holder. The center square region is for spotting. (c) Image of an antibody spot on the prototype.

reintroduced with single-molecule detection capabilities [17]. Utilizing a silicon-oxide on silicon sensor, this platform exploits the common path interference between the scattering field of a nanoparticle and the multilayer reflection from the sensor. Further analysis of the detected signal has shown to yield additional information about the size, material, shape, and nanoparticle aspect ratio [17]–[19] to identify the target molecules in the presence of nonspecific binding. The digital detection scheme and orthogonal verification measurements enable a dramatic increase in the sensor's detection limit compared to traditional ensemble measurement techniques, such as fluorescence, in both serum and whole-blood [20]. In this paper, we present an automated and easy-to-use biosensor imaging platform (see Fig. 1) using the single particle detection modality which we term the single particle interferometric reflectance imaging sensor (SP-IRIS).

II. METHODS

For a biosensor platform to be successfully translated from a research laboratory environment, it must be either automated (to enable use by an untrained operator), or it should utilize a simple operating process (e.g., glucose meter). Be it a primary physician office (bedside), home (personal), or a low-resource location (global health), the optimal design must take into consideration the effect of environmental and infrastructural constraints. In the case of a portable SP-IRIS instrument for a primary physician office, the design must give priority to: 1) instrument size; 2) vibration isolation; 3) simplicity; 4) cost; and 5) automation. To achieve a robust, compact, and simple platform, off-the-shelf optical and electrical components have been merged with custom mechanical parts and robust software.

A. SP-IRIS Detection Principle

Optical detection of protein, DNA, and viruses is challenging due to their small size, weakly scattering cross section, and low index contrast to the surrounding medium. Classical scattering theory describes the signal strength of light scattered off of a particle as dipoles induced on a nonabsorbing particle [21]. The scattered electrical field E_{sca} is proportional to the particle polarizability α:

$$E_{sca} \propto \alpha = 4\pi\varepsilon_0 r^3 \frac{\varepsilon_p - \varepsilon_m}{\varepsilon_p + 2\varepsilon_m} \qquad (1)$$

where r is the particle radius and $\varepsilon_0, \varepsilon_p$, and ε_m are the free space, particle, and surrounding medium permittivity, respectively. Scattering-based detection techniques therefore have a detected signal $I \propto |E_{sca}|^2$ which scales by $|r^3|^2 \propto r^6$. In other words, comparing a 1-μm bacterium to a 100-nm viral particle, the signal drops by 1 million fold and disappears into the detector's noise. As explained by Daaboul *et al.* [17], the particle's signal can be strengthened through the use of interferometry. The interference of the particle's scattering field with the reference field E_{ref} gives the following far-field response

$$I_{det} \propto |E_{sca} + E_{ref}|^2 = |E_{sca}|^2 + |E_{ref}|^2$$
$$+ 2|E_{ref}||E_{sca}|\cos\theta_{rs} \qquad (2)$$

where θ_{rs} refers to the phase-angle difference between the fields, and I_{det} is the intensity of the far-field response. In this case, $|E_{sca}|^2$ is equivalent to the previous case and will be negligibly small; $|E_{ref}|^2$ contributes a constant background intensity, and the third interference term forms the dominant optical response of the nanoparticle. By interfering the scattered field and reference field, the signal now scales by the radius cubed.

SP-IRIS utilizes a common-path interferometer to create a compact and robust platform with an improved dynamic range and sensitivity to nanoparticles, over pure scattering modalities. Further analysis of the detected signal as a function of signal strength, wavelength response, defocus response, and polarization response yields information about the particle size, shape, and material [17], [18]. SP-IRIS utilizes these additional methods of particle identification to eliminate false signals from nonspecific binding.

B. Hardware Design

In the following discussion, the parts and materials of individual design elements (the sensor chip, the optics, the electronics, and the mechanics) are given. For each design component, the specific part numbers are provided. These components were selected to meet or exceed design requirements.

1) Sensor Chip Design: For silicon oxide on silicon substrates, a thickness of 100 nm has been selected to maximize the phase angle term [19]. Silicon chips with thin layers of silicon oxide, fabricated by SVMI, Inc. (Santa Clara, CA, USA), were designed to be used with a reusable loading holder. Fiduciary patterns enable the use of an automatic spot detection algorithm, in addition to providing contrast for autofocusing algorithms. The dimensions of the chips are 10 mm × 10 mm × 0.5 mm, with a 2.3 mm × 2.3 mm active center region for spotting capture probes. Small, periodic etched squares (15 μm × 15 μm every 143 μm) in the capture probe area ensure that regions of high contrast are present in the field of view for coarse focusing, independent of the precise location of each capture probe spot.

2) Optical Design: The SP-IRIS technique is based on a top-illumination microscope scheme. The key parameters in the optical path design are the illumination wavelength, uniformity, numerical aperture (NA), magnification, and camera pixel size. These parameters determine the accuracy of sizing, throughput, and minimum detection size of the system.
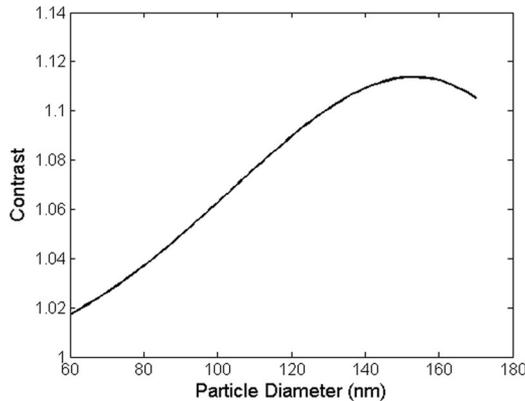
Fig. 2.   Interferometric particle response. Simulated response of viral nanoparticles to a 528 nm center wavelength source. A contrast of one corresponds to an unperturbed background response.
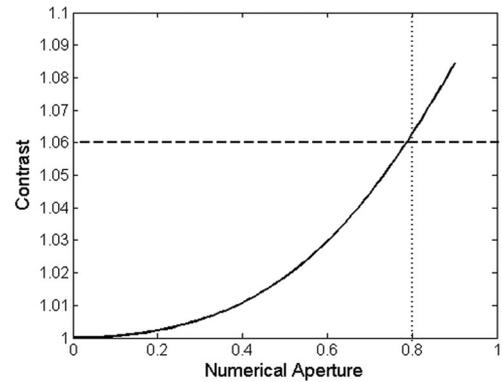

Fig. 3.   Theoretical response of a 100 nm virus when the NA of the objective is varied. The dashed horizontal bar indicates an SNR of three above the background noise. The dotted vertical line indicates the selected NA, 0.8.

In imaging systems, the uniformity of illumination is vital to obtain a comparable performance across the sensor. For the SP-IRIS technique, improper illumination will affect the detection and sizing capabilities. In particular, because sizing is calculated via contrast of the central peak to near-neighbor background pixels, nonuniformity of the illumination will introduce sizing ambiguity. For light-emitting diodes (LEDs) and filament sources, uniform illumination is achieved through either the Nelsonian illumination or Kohler illumination. The Nelsonian illumination requires only a condenser lens; however, this approach typically includes an image of the illumination source in the image plane. The Kohler illumination scheme contains an additional lens but overcomes the issue of the illumination source image for a smoother image. Since sizing depends on uniform illumination, the Kohler illumination scheme is deployed in this design.

Wavelength selection drives the system's sizing capabilities. As shown previously by Daaboul *et al.*, the effective range and accuracy of nanoparticle sizing are greatly affected by the illumination wavelength [17]. In this prototype, a 528-nm LED is used to directly detect 60–160 nm viral particles by their simulated contrast values (see Fig. 2).

Adjusting the NA offers a tradeoff between nanoparticle contrast and usable field of view. The image of the nanoparticle is calculated from a forward model that is derived using the angular spectrum representation, where the nanoparticles are modeled as dipoles to determine the expected far-field signal of the virus [22]. To ensure reliable detection of the virus, an NA offering a signal-to-noise ratio (SNR) of at least 3 over the background noise was selected. Fig. 3 shows the contrast response of a 100-nm virus (equivalent to H1N1) and the peak of the response as a function of NA. Particle sizing in the SP-IRIS technique is performed by comparing the detected particle peak contrast to the predictive forward model. A potential source of error in this comparison is undersampling of the point spread function (PSF). Defining the minimum separation according to the Rayleigh criterion, the calculated PSF of the system is 400 nm for the prototype. If the resolution of the camera undersamples the PSF, the central peak of a nanoparticle's PSF could be blurred between multiple pixels. To guarantee proper imaging of the PSF, an oversampling rate of at least 3 is recommended which, in this case, corresponds to an effective pixel size of 138 nm × 138 nm. This system meets this requirement with a 50×, 0.8 NA Nikon objective and the Grasshopper 2 GigE CCD camera (Point Grey Research, Inc., BC, Canada) with 2 × 2 binning. The resulting optical parameters are an effective pixel size of 138 nm × 138 nm and a total field of view of 168 μm ×141 μm.

3) Electrical Design: For rapid system development, an attempt was made to maximize the use of commercial off-the-shelf subcomponents. This included a Gigabit Wireless Router (AirStation HighPower N450 Gigabit Wireless Router, Buffalo Technology, Inc., Austin, TX, USA), an industrial serial RS232 to Ethernet Converter (BF-431, Gridconnect Inc., Naperville, IL, USA), a high-power LED (Golden Dragon LT W5 SM, OSRAM Opto Semiconductors), and a high-speed Gigabit CMOS Camera (GS2-GE-50S5M-C, Point Grey Research, Inc., Richmond, BC, Canada).

To integrate all these components together inside the SP-IRIS enclosure some custom electronics were needed, to control the LEDs and generate the necessary supply voltages for all subcomponents from the single 24 V dc power supply. To save space, four 64 mm × 64 mm, four-layer printed circuit boards were vertically stacked and connected through a 26-pin cable. Each board served a single purpose: high efficiency regulation of the necessary 12 and 5 V power supplies, constant current led driving circuits (TL4242, Texas Instruments Inc., Austin, TX, USA), Ethernet to UART interface, and a microcontroller (MSP430AFE221, Texas Instruments Incorporate, Austin, TX, USA) to allow TCP/IP commands to be issued to control the LEDs.

By using a gigabit router for all communications to subcomponents, standard TCP/IP networking protocols were used over 10/100/1000 Mbit Ethernet with category-6 unshielded twisted pair cables. This allows a single interface for communication with components and will enable a seamless transition to high-speed wireless interfaces (802.11n) for control and interfacing. The system uses a peak power of 29 W during power-up and acquisition, and 23–24 W while idle.

4) Mechanical Design: A field of view of 168 μm $\times$ 141 μm and a focus dependent particle sizing introduces the potential for cross-dataset variability, as small differences in operator technique can result in significant divergence in particle counts. Designing an operator independent protocol is vital for POC devices. The mechanical design of the system solves the issue with rigidity and automation.

The SP-IRIS prototype utilizes a 3-axis orthogonal stack of linear stages (VT-21, Micos, Irvine, CA, USA) to enable the rapid scanning of samples. A removable chip holder secures the sensor in a repeatable location with a spring-loaded latch. The holder is then secured to the stage assembly via a series of alignment pins and magnetic retention features. Fine alignment adjustments are enabled via a pitch / yaw mechanism built into the stage assembly.

All required optics, mechanics, and electronics are incorporated inside a robust and portable envelope measuring 43 cm $\times$ 28 cm $\times$ 20 cm. An aluminum base plate equipped with vibration dampening feet provides a stable mounting platform for all onboard components and doubles as a heat sink for the stage components.

C. Software Design

The user interface of a POC diagnostic instrument must be easy to use. Ideally, an untrained operator should be able to use the instrument with a simple set of instructions. Creating an easy-to-use interface requires a high level of mechanical and software automation. Applying these criteria to a high-resolution optical technique requires engineering in both image acquisition and image processing. In the analysis of microarray assays, the time to process each spotted condition becomes the determining factor behind measurement time. Here, an easy-to-use user interface and the novel image processing algorithms to achieve acquisition times less than 1 min per spotted condition are presented.

1) Graphical User Interface: Incorporating a simple, easy-to-use, and readable user interface is pivotal in developing a tool for POC settings. In these environments, the target user cannot be required to have specialized training. With the algorithms discussed in the following sections, the SP-IRIS instrument is able to achieve a 5-click interface, as shown in Fig. 4. This interface requires user interaction only for loading/unloading and basic array information. Once the user clicks acquire and analysis, the software precedes spot to spot acquiring data. The first spot of the array is located through the use of fiducial marks and subsequent spots are found through the user defined spot pitch. At each spot, the instrument executes the focus algorithms described in the following sections. Once focused, the number of viral particles detected is tallied and recorded in the table.

2) Particle Detection: Robust, rapid, and automated particle detection is an enabling feature of an easy-to-use SP-IRIS interface. The detection of the sparse nanoparticle diffraction patterns in the image requires the implementation of several image processing techniques. To start, an important observation is these nanoparticles are well localized and local extrema in the pixel space. A profile of a 100-nm viral nanoparticles is shown
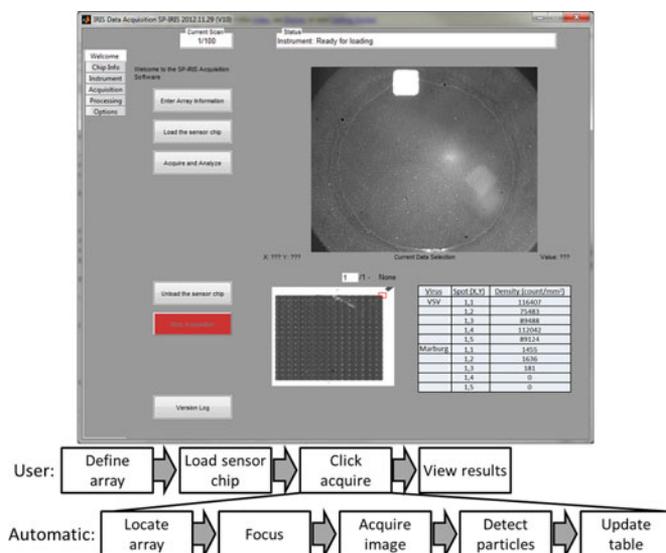

Fig. 4. User Interface. The software shown here simplifies acquisition and analysis for untrained to minimally trained users. The user defines the array geometry (array size and spot pitch), loads the sensor chip, and then clicks once for acquisition and analysis. When the instrument finishes, results are reported in the table and saved into a spreadsheet. Additional functionalities are included in other tabs for advanced users but not required for typical operation.
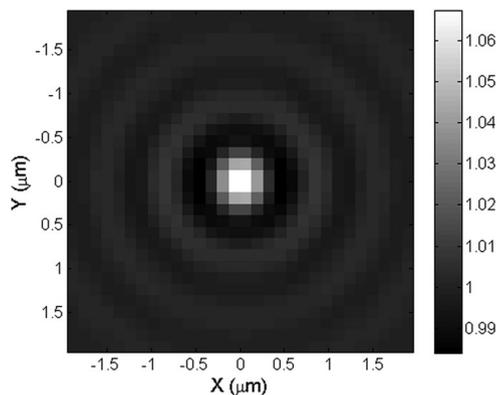

Fig. 5. Simulated response of a 100 nm spherical viral particle in the SP-IRIS system.

in Fig. 5. Such features are the characteristic of an interest point in computer vision. Interest point detection is a well-studied subject, and tools from the existing literature have been adapted for robust detection of the nanoparticles. Scale invariant feature transform (SIFT) has been proven to be one of the most robust interest point detection methods and has been used in this study [23].

Interest points exist at many different scales in a natural image. Likewise, in SP-IRIS images, a particle's response can change, depending on the particle type and size. Furthermore, experimental variables such as magnification, pixel size, NA, and particle defocus lead to different particle profiles. Given the wide experimental conditions, it would be restrictive to search particles at a fixed scale. SIFT resorts to scale-space methods to eliminate the problem of identifying the correct scale of the interest points.
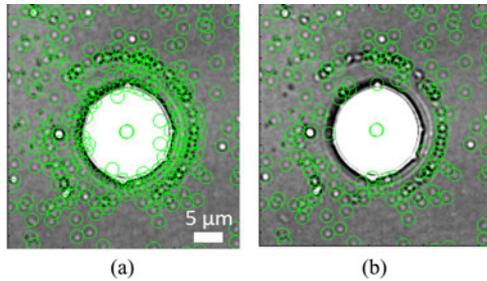
Fig. 6. Nanoparticle filtering at artifact edges is illustrated with these cropped images. (a) Expected gradient behavior is relaxed leading to a large number of false signals near the artifact edge. (b) Tightening the constraint eliminates these false-edge signals
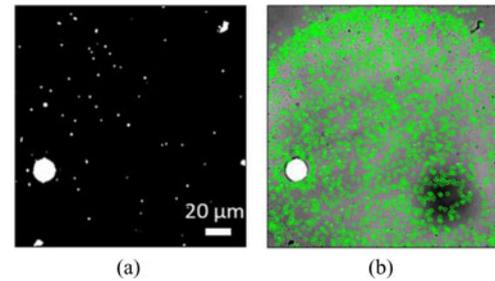

Fig. 7. Anomaly Filtering. (a) Detected anomaly map of nonspecific structures. (b) Using the anomaly map to discard particles within those regions, the nanoparticles of interest (green circles) are accurately identified.

Scale-space methods form a multiresolution representation of an image by incremental smoothing. A Gaussian kernel is used for smoothing since it has been found that it does not introduce any spurious artifacts as the image is smoothed [24]. As smoothing is applied the image can be subsampled since high-frequency information is reduced. The resulting image stack is called a pyramid representation. Given this scale-space pyramid representation, the SIFT detector computes the difference-of-Gaussian function and treats scale-space extrema as potential interest points.

Each pixel in the difference-of-Gaussian scale space representation is compared with its 26 neighboring pixels: eightpixels on the same scale and 18 pixels from lower and upper scales. A pixel is identified as a potential interest point if it is an extremum with respect to its neighbors. Once a pixel is identified as a potential interest point, it is parameterized and evaluated in its neighborhood. In particular, the SIFT detector fits a 3-D quadratic function using the parameters of the potential interest point, local gradient, and Hessian information. The evaluation of the extremum of this function facilitates subpixel localization of the interest point in the scale space. Furthermore, the function value at the extremum is used to eliminate unstable and low contrast interest points. The details of the SIFT technique can be found in [23].

In the case of large artifacts, nanoparticle responses near the boundary of the artifact can exhibit unexpected behavior. These particles are eliminated through the use of the corner-detection method proposed by Harris and Stephens in SIFT [25]. The Harris detector measures the corner response of an interest point by evaluating the gradient information in its neighborhood. A 2×2 second moment matrix is calculated using image derivatives, and a comparison of eigenvalues of this matrix are used to assess the eccentricity of an interest point and its neighborhood. Interest points with a strong gradient in all directions have their second moment matrices with large and close eigenvalues, whereas interest points that are on edges have one large and one small eigenvalue. As seen in Fig. 6, when the gradient behavior is relaxed many false structures are identified as particles. However, by increasing this constraint, the false signals are eliminated.

In SP-IRIS images, given the particle type of interest and other experimental variables, the forward model is computed and the expected normalized peak response of the particles of interest
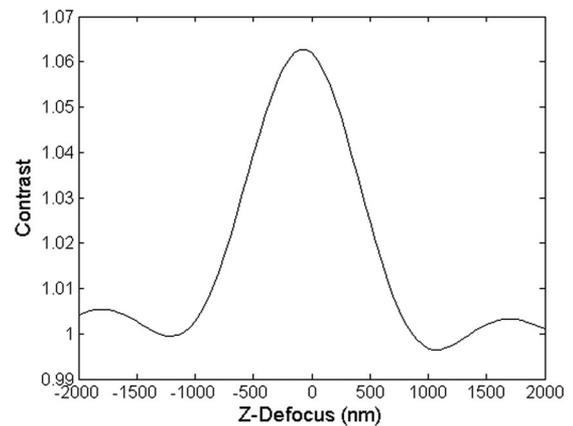
Fig. 8. Simulated response of a 100 nm spherical virus at different z-planes. The sensor surface is defined as $z = 0$. The detectable window (contrast >1.02) is between -700 and 500 nm with the peak response occurring at -100 nm.

is known. For example, if one aims to image 100-nm viral nanoparticles, the expected normalized peak value would be around 1.06. This information is used to eliminate strong interest points that are related to salts and large nonspecifically bound particles. In order to detect strong interest points, the ratio of the maximum to minimum value of a pixel in its local neighborhood is computed and thresholding is used to find regions with high-intensity differences. The resulting binary image is named as the anomaly map. Fig. 7 shows the detection and elimination of anomaly region. Note that for sizable anomalous structures, the pixels toward the center of the large structures do not have a high-intensity difference. In order to overcome this, a morphological close operation is used to fill such gaps in sizable structures.

3) Closed-Loop Focusing: The automation of optical devices requires the use robust autofocusing. For POC devices, a robust, precise, and real-time algorithm is imperative to minimize experimental time and prevent erroneous results. Choosing the correct passive autofocusing algorithm weighs heavily on the imaging modality and the target object [26]. For some applications, the sample alignment conditions are loose. However, in the case of SP-IRIS, focusing is critical as the response of the nanoparticle rapidly peaks, as shown in Fig. 8. The challenge of a rapid focusing algorithm is compounded by two issues: 1) a narrow detectable window where the nanoparticle contrast is above the background and 2) the optimal focal plane of the nanoparticles does not coincide with the sensor surface.

To approach the autofocusing for the SP-IRIS technique in a robust, rapid manner, two complementing algorithms have been implemented.

When the sensor is loaded, the removable chip holder latches into the stage assembly. Since the nanoparticle detection window overlaps with the sensor surface, the coarse focusing algorithm is executed to bring the imaging plane to the sensor surface by focusing on the 15 μm square fiduciary marks within the field of view. The stages are swept 30 μm acquiring an image every micrometer. A fast Fourier transform is applied to the stack of the images followed by a high-pass filter. The remaining high frequencies are summed. The most in-focus plane corresponds to the maximum sum. With the stages now within 2 μm of the sensor surface focal plane, the algorithm is reiterated over 2 μm with 100 nm steps. The resulting in-focus plane is somewhere within the nanoparticle detection window.

For repeatable sizing, a nanoparticle detection feedback algorithm is executed to locate the nanoparticle peak contrast plane. This algorithm swings from -300 to $+300$ nm of the current location by 100 nm increments acquiring images. Each image is then processed to detect and size the detected nanoparticles. The optimal focal plane is determined by maximizing the number of particles within the desired particle size range. This algorithm in combination with the coarse focus requires less than 90 s.

These algorithms have shown high repeatability in clean data. Nevertheless, nonspecific binding and salt occur in nonideal laboratory settings. Anticipating the situations where nonspecific binding will bias the high-pass filter autofocus algorithm to the wrong starting plane, the algorithm also performs shifting window detection. If the optimal plane is determined to be at either extreme of the current window, the focal planes being analyzed will be shifted. The new window of focal planes will be acquired and processed. Shifting the focal plane increases the robustness of the autofocusing but at a cost of time. To prevent runaway situations, the number of iterations is limited to four per spot giving a total analysis range of 2.2 μm to the nanoparticle detection feedback algorithm.

III. CHARACTERIZATION

A. Proof of Concept

Clinical diagnostic tests are rarely performed with a simple sample solution. Typically, biomarker analytes are vastly outnumbered by endogenous proteins and macromolecules found in unprocessed patient samples, ensuring that the diagnostic assay can specifically and sensitively detect the target within a complex solution, which is imperative. The presence of other macromolecules can lead to nonspecific binding which decreases the test confidence. A proof-of-concept experiment showing specific detection of wildtype vesicular stomatitis virus (wtVSV), a biosafety level 2 pathogen, spiked in 100% fetal bovine serum (FBS) is performed. To ensure that the constructed prototype operates in a comparable capacity to our laboratory system, this experiment is also used as a benchmark.

An antibody against the wtVSV surface glycoprotein (8G5 monoclonal antibody) and a negative control monoclonal antibody (specific for the Marburg virus glycoprotein) were arrayed
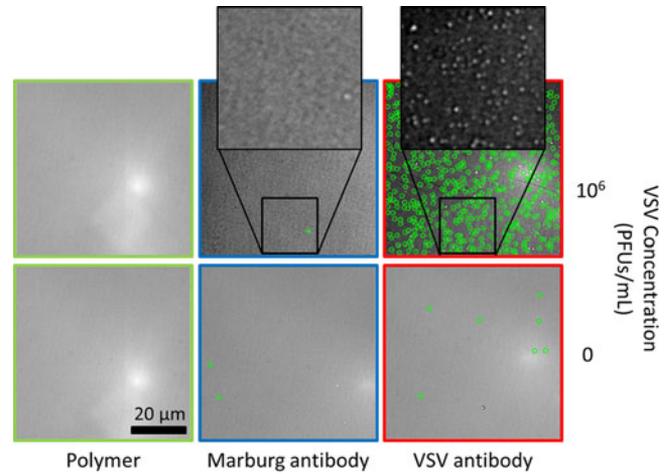

Fig. 9. Specific virus capture and detection. The panels show detection of wtVSV (circled in green) for 0 and 10^6 PFU/ml concentrations in 65 μm $\times$ 65 μm area.

onto the sensor described in Section B-I, which is functionalized with the MCP-2 co-polymer from Lucidant Polymers LLC (Sunnyvale, CA, USA). The array printed by the sciFlexarrayer S3 spotter (Scienion AG, Berlin, Germany) consisted of five replicates of each antibody. After an overnight incubation, the surface was first treated with 50-mM ethanolamine (pH 8), then washed with phosphate buffered saline (PBS) containing 0.1% tween-20 to remove any remaining unbound material followed by blocking for 1 h in a petri dish with 1% bovine serum albumin with PBS. Finally, the sensors were thoroughly rinsed in deionized water to remove salt. The images of the resulting antibody spots were acquired on both the prototype and laboratory platforms to determine the number of preincubation bound particles. Next, the sensor was incubated in another petri dish with undiluted FBS spiked with 5×10^5 plaque-forming units per milliliter (PFU/mL) of wtVSV for 2 h. Following the incubation, the sensor was washed with PBS and rinsed quickly in deionized water. Finally, postincubation images of the spotted array were acquired. Fig. 9 shows the specific detection of 100 to 140 nm diameter particles in the postincubation images of SP-IRIS prototype. VSV is bullet shaped (80 nm $\times$ 160 nm); however, when imaging with nonpolarized light, the average polarizability which is equivalent to a spherical particle with a 110 nm diameter is observed [18], [19]. The comparison of the two platforms was conducted via the detected density of the wtVSV particles on both the wtVSV-specific and Marburg-specific antibody spots. Fig. 10 demonstrates that the prototype is able to detect virus particles trapped on the wtVSV-recognizing antibody with little to no binding on the non-specific spot. An equal density between the platforms illustrates no loss in sensitivity.

IV. DISCUSSION AND CONCLUSION

POC diagnostic tests have the potential to revolutionize primary care treatment. The translation of laboratory diagnostic tests to the bedside has the potential to reduce medical costs, while providing the primary care physician with supplementary information for more accurate diagnoses. In cases of early viral
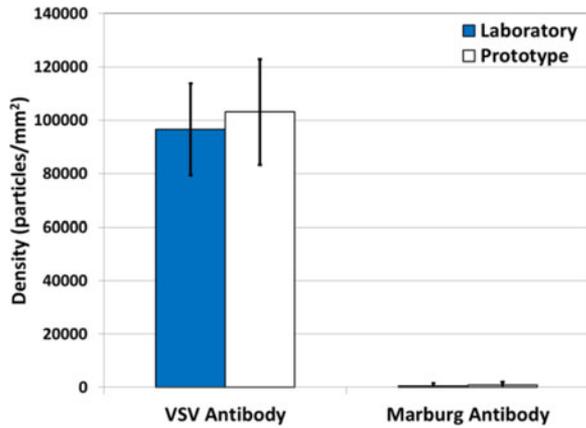
Fig. 10. Benchmark comparison for 5×10^5 PFU/mL of wtVSV. Identical areas of the wtVSV antibody and controls spots were analyzed on the prototype and laboratory SP-IRIS platforms. The number of particles detected between 90 and 140 nm were tallied. The mean and standard deviation for each condition were determined from particle counts on five replicate spots.

detection, these diagnostic tests cannot rely upon the detection of antibodies but the virus directly.

This paper presents the development and characterization of an automated SP-IRIS platform capable of multiplexed pathogen detection at a clinically relevant sensitivity. The SP-IRIS detection method has the capability to detect single binding events on the interferometric surface. The specificity of the probe-target binding is supplemented by a size-discrimination algorithm to enhance the limit of detection of this technique beyond traditional detection methods [20].

The automation of the acquisition and processing enables minimally trained operation or untrained user operation. The user interface sports a simple 4-button interface and tabular readout for ease of use. System validation against the laboratory platform was confirmed for whole virus detection at a clinically relevant level (5×10^5 PFU/ml) of wtVSV spiked in undiluted FBS.

The presented automated platform is the first step toward reliable assays in the physician's office to stem the spread of infectious diseases. As a POC viral diagnostic platform, the automation of these steps demonstrates the plausibility of SP-IRIS with the incorporation of sample preparation. Future designs will eliminate the need to enter the array geometry by building a reference database for the chip ID and incorporate a microfluidic sample preparation cartridge for a complete sample-to-answer platform. For additional verification beyond specific binding, material identification through focusing, and shape discrimination, the next design iteration will also incorporate the polarization calculations demonstrated in previous publications [18].

REFERENCES

[1] A. Rajan and H. Glorikian, "Point-of-care diagnostics: Market trends and growth drivers," *Expert Opin. Med. Diagnos.*, vol. 3, no. 1, pp. 1–4, 2009.

[2] M. Debnath, G. B. K. S. Prasad, and P. S. Bisen, "Segments of molecular diagnostics—Market place," in *Molecular Diagnostics: Promises and Possibilities.* Dordrecht, The Netherlands: Springer, 2010, pp. 503–513.

[3] Y. J. Choi, H. S. Nam, J. S. Park, H. J. Kim, K. B. Park, M. H. Jeon, C. J. Kim, Y. Hwangbo, K. S. Park, and K. A. Baek, "Comparative analysis of the multiple test methods for the detection of pandemic influenza A/H1N1 2009 Virus," *J. Microbiol. Biotechnol.*, vol. 20, no. 10, pp. 1450–1456, Oct. 2010.

[4] C. Chartrand, M. M. G. Leeflang, J. Minion, T. Brewer, and M. Pai, "Accuracy of rapid influenza diagnostic tests: A meta-analysis," *Ann. Internal Med.*, vol. 156, pp. 500–511, 2012.

[5] S. A. Harper, J. S. Bradley, J. A. Englund, T. M. File, S. Gravenstein, F. G. Hayden, A. J. McGeer, K. M. Neuzil, A. T. Pavia, M. L. Tapper, T. M. Uyeki, and R. K. Zimmerman, "Seasonal influenza in adults and children - diagnosis, treatment, chemoprophylaxis, and institutional outbreak management: Clinical practice guidelines of the Infectious Diseases Society of America," *Clin. Infect. Dis.*, vol. 48, no. 8, pp. 1003–1032, Apr. 2009.

[6] B. T. Cunningham and R. C. Zangar, "Photonic crystal enhanced fluorescence for early breast cancer biomarker detection," *J. Biophoton.*, vol. 8–9, pp. 617–628, Jun. 2012.

[7] M. A. Santiago-Cordoba, M. Cetinkaya, S. V Boriskina, F. Vollmer, and M. C. Demirel, "Ultrasensitive detection of a protein by optical trapping in a photonic-plasmonic microcavity," *J. Biophoton.*, vol. 638, no. 8, pp. 629–638, Jun. 2012.

[8] V. R. Dantham, S. Holler, V. Kolchenko, Z. Wan, and S. Arnold, "Taking whispering gallery-mode single virus detection and sizing to the limit," *Appl. Phys. Lett.*, vol. 101, no. 4, pp. 043704–043708, 2012.

[9] H. Zhu, S. O. Isikman, O. Mudanyali, A. Greenbaum, and A. Ozcan, "Optical imaging techniques for point-of-care diagnostics," *Lab Chip*, vol. 13, pp. 51–67, Oct. 2012.

[10] B. Veigas, J. M. Jacob, M. N. Costa, D. S. Santos, M. Viveiros, J. Inácio, R. Martins, P. Barquinha, E. Fortunato, and P. V. Baptista, "Gold on paper–paper platform for Au-nanoprobe TB detection," *Lab Chip*, vol. 12, no. 22, pp. 4802–4808, Oct. 2012.

[11] O. Mudanyali, S. Dimitrov, U. Sikora, S. Padmanabhan, I. Navruz, and A. Ozcan, "Integrated rapid-diagnostic-test reader platform on a cellphone," *Lab Chip*, vol. 12, no. 15, pp. 2678–2686, Aug. 2012.

[12] F. Ahmad and S. A. Hashsham, "Miniaturized nucleic acid amplification systems for rapid and point-of-care diagnostics: A review," *Analytica Chimica Acta*, vol. 733, pp. 1–15, Jul. 2012.

[13] M. D. Estes, J. Yang, B. Duane, S. Smith, C. Brooks, A. Nordquist, and F. Zenhausern, "Optimization of multiplexed PCR on an integrated microfluidic forensic platform for rapid DNA analysis," *Analyst*, vol. 137, no. 23, pp. 5510–5519, Dec. 2012.

[14] A. Puren, J. L. Gerlach, B. H. Weigl, D. M. Kelso, and G. J. Domingo, "Laboratory operations, specimen processing, and handling for viral load testing and surveillance," *J. Infect. Dis.*, vol. 201, no. Suppl. 1, pp. S27–S36, 2010.

[15] G. G. Daaboul, R. S. Vedula, S. Ahn, C. A. Lopez, A. Reddington, E. Ozkumur, and M. S. Ünlü, "LED-based interferometric reflectance imaging sensor for quantitative dynamic monitoring of biomolecular interactions," *Biosens. Bioelectron.*, vol. 26, no. 5, pp. 2221–2227, Jan. 2011.

[16] C. A. Lopez, G. G. Daaboul, R. S. Vedula, E. Ozkumur, D. A. Bergstein, T. W. Geisbert, H. E. Fawcett, B. B. Goldberg, J. H. Connor, and M. S. Ünlü, "Label-Free multiplexed virus detection using spectral reflectance imaging," *Biosens. Bioelectron.*, vol. 26, no. 8, pp. 3432–3437, Apr. 2011.

[17] G. G. Daaboul, A. Yurt, X. Zhang, G. M. Hwang, B. B. Goldberg, and M. S. Ünlü, "High-throughput detection and sizing of individual low-index nanoparticles and viruses for pathogen identification," *Nano Lett.*, vol. 10, no. 11, pp. 4727–4731, Nov. 2010.

[18] A. Yurt, G. G. Daaboul, J. H. Connor, B. B. Goldberg, and M. S. Ünlü, "Single nanoparticle detectors for biological applications," *Nanoscale*, vol. 4, no. 3, pp. 715–726, Feb. 2012.

[19] G. G. Daaboul, C. A. Lopez, A. Yurt, B. B. Goldberg, J. H. Connor, and M. S. Ünlü, "Label-Free optical biosensors for virus detection and characterization," *IEEE J. Sel. Topics Quantum Electron.*, vol. 18, no. 4, pp. 1422–1433, Jul./Aug. 2012.

[20] M. R. Monroe, G. G. Daaboul, A. Tuysuzoglu, C. A. Lopez, F. F. Little, and M. S. Ünlü, "Single nanoparticle detection for multiplexed protein diagnostics with attomolar sensitivity in serum and unprocessed whole blood," *Analytical Chem.*, vol. 85, no. 7, pp. 3698–3706, 2013.

[21] C. F. Bohren and D. R. Huffman, *Absorption and Scattering of Light by Small particles*. New York, NY, USA: Wiley, 1998.

[22] L. Novotny and B. Hecht, *Principles of Nano-optics*. Cambridge, U.K.: Cambridge Univ. Press, 2006.

[23] D. G. Lowe, "Distinctive image features from scale-invariant keypoints," *Int. J. Comput. Vis.*, vol. 60, no. 2, pp. 91–110, Nov. 2004.

[24] T. Lindeberg, "Scale-Space Theory : A basic tool for analysing structures at different scales," *J. Appl. Statist.*, vol. 21, no. 2, pp. 224–270, 1994.

[25] C. Harris and M. Stephens, "A combined corner and edge detector," in *Proc. 4th Alvey Vis. Conf.*, 1988, pp. 147–152.

[26] J. M. Mateos-Pérez, R. Redondo, R. Nava, J. C. Valdiviezo, G. Cristóbal, B. Escalante-Ramírez, M. J. Ruiz-Serrano, J. Pascau, and M. Desco, "Comparative evaluation of autofocus algorithms for a real-time system for automatic detection of mycobacterium tuberculosis," *Cytometry Part A : J. Int. Soc. Advancement Cytometry*, vol. 81, no. 3, pp. 213–221, Mar. 2012.

Alexander P. Reddington (S'06) received the B.S. degree in electrical engineering from West Virginia University, Morgantown, WV, USA, in 2008 and the M.S. degree in electrical engineering from Boston University, Boston, MA, USA, in 2012. He is currently pursuing the Ph.D. degree in electrical engineering from Boston University with Professor M. Selim Ünlü at the Optical Characterization and Nanophotonics (OCN) Laboratory.

His research interest lies in optical instrumentation development, more specifically label-free biosensors for translational applications.

Jacob T. Trueb received the B.S. degree in mechanical engineering from Tufts University in 2008 and the M.S. degree in mechanical engineering from Boston University, Boston, MA, USA, in 2011. He is currently pursuing the Ph.D. degree in mechanical engineering from Boston University, Boston, MA, USA with Professor M. Selim Ünlü at the Optical Characterization and Nanophotonics (OCN) Laboratory.

His research interests lie in the design and automation of microfluidic lab-on-chip diagnostic platforms.

David S. Freedman (M'12) received the B.S. degree in electrical engineering and the B.A. degree in economics from the University of California, San Diego, La Jolla, CA, USA, in 2005, and the Ph.D. degree in electrical engineering from Boston University, Boston, MA, USA, in 2010 from the VLSI and Neural Net Systems (VNNS) Laboratory.

He is currently a Research Engineer at the Center for Neuroscience, Boston University, where his research goals are to develop wireless brain machine interfaces. Prior to that, he was a Postdoctoral Researcher with Professor M. Selim Ünlü at Boston University's Optical Characterization and Nanophotonics (OCN) Laboratory where he developed addressable optically powered neural stimulators for use in the spinal cord.

Ahmet Tuysuzoglu (S'06–M'08–S'13) photograph and biography not available at the time of publication.

George G. Daaboul, photograph and biography not available at the time of publication.

Carlos A. Lopez, photograph and biography not available at the time of publication.

W. Clem Karl (S'83–M'87–SM'00) photograph and biography not available at the time of publication.

John H. Connor, photograph and biography not available at the time of publication.

Helen Fawcett, photograph and biography not available at the time of publication.

M. Selim Ünlü (S'90–M'91–SM'95–F'07) photograph and biography not available at the time of publication.